CNRS
Centre National de la Recherche Scientifique

INFN
Istituto Nazionale di Fisica Nucleare

Simulation of the angular sensing for the Central Interferometer in Advanced Virgo+

VIR-0349A-21

M. Boldrini[*1], J. Casanueva[2], M. Mantovani[2], and E. Majorana[1]

[1] *INFN - Sezione Roma 1*
[2] *EGO - European Gravitational Observatory*

Date: April 28, 2021

[*] *corresponding author:*

VIRGO* A joint CNRS-INFN Project
Via E. Amaldi, I-56021 S. Stefano a Macerata - Cascina (Pisa)
Secretariat: Telephone (39) 050 752 521 * FAX (39) 050 752 550 * Email: ego@ego-gw.it

Contents

1 Introduction

The goal of this work is to find the best angular sensing for the central ITF (CITF) for AdV+ by taking into account the sensing matrix components, the linear region of each error signal and the coupling among the signals for any given DoF.
AdV+ is simulated in its dual recycled configuration with the 40 W of injected power.
To study the CITF, the phase accumulated by the carrier field on reflection on the ETMs is set to be 30° in the simulation, which represents a condition approximately half way between the resonance conditions of the carrier and the 6 MHz sidebands, in order to avoid crossing a resonance by accident for any movement of the other mirrors.
The remaining optical configuration consists of the Power and Signal Recycling mirrors (PR and SR), and the West and North Input mirrors (WI and NI).
To build the angular sensing matrix, we are going to model the response of the sensor while sweeping each angular DoF at a time, while keeping every longitudinal DoF at its working point. At the same time we plot both the DC and the demodulated signal detected by a set of quadrant photodiodes.
In principle, to determine the optical gain of each error signal it would be sufficient to compute its frequency response to the excitement of each DoF and take the low frequency gain, but this would yield no information about other critical aspects of the error signal, like the existence of multiple zero-crossing, the presence of some offset or the width of the linear region. By sweeping them instead, we can obtain all of these information. and build the control scheme for the angular control.

2 Simulation tools

2.1 Simulated CITF

As stated, this simulation work was focused on the CITF:

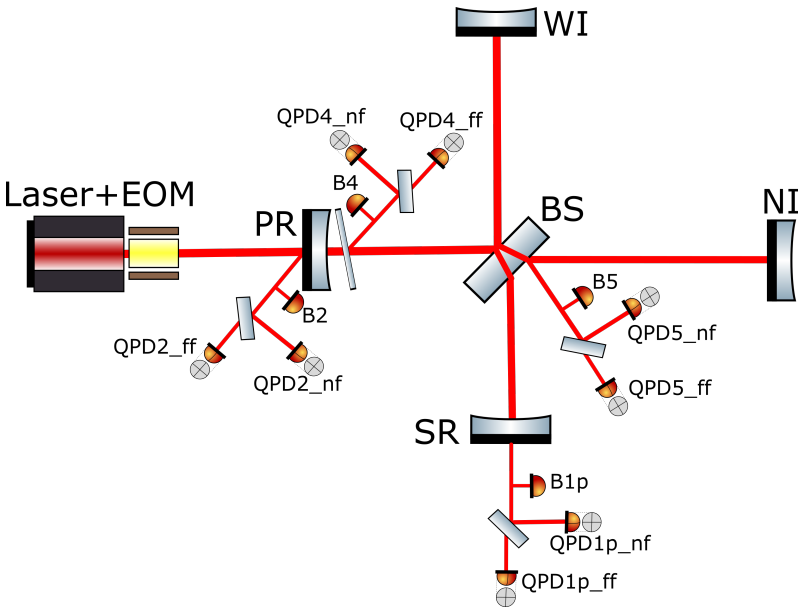

Figure 1: Representation of the Central ITF (CITF) used for the simulation work, complete with PDs and QPDs used to simulate the error signals. Finesse allows to attach photodiodes of any kind directly "on" the beam, without the need to pick it off with a beam splitter. Each QPD is preceded by a space where the Gouy phase of the beam has been set to 0° (for **nf** QPDs) or 90° (for **ff** QPDs).

Notice that for Finesse a realistic positioning of the components is irrelevant. Every component of the simu-

lated interferometer is connected to each other via nodes, but apart from that there is no other information on their relative positioning, and parameters like the reflection angle on a surface are set when each component is declared. That is why in Fig.1 the positioning of B2 and B5 sensors do not represent reality.

Furthermore, the carrier field is modulated at these frequencies:

- **f1** = 6270777 Hz
- **f2** = 56436993 Hz
- **f3** = 8361036 Hz

with the following resonances conditions for the corresponding sidebands (SBs):

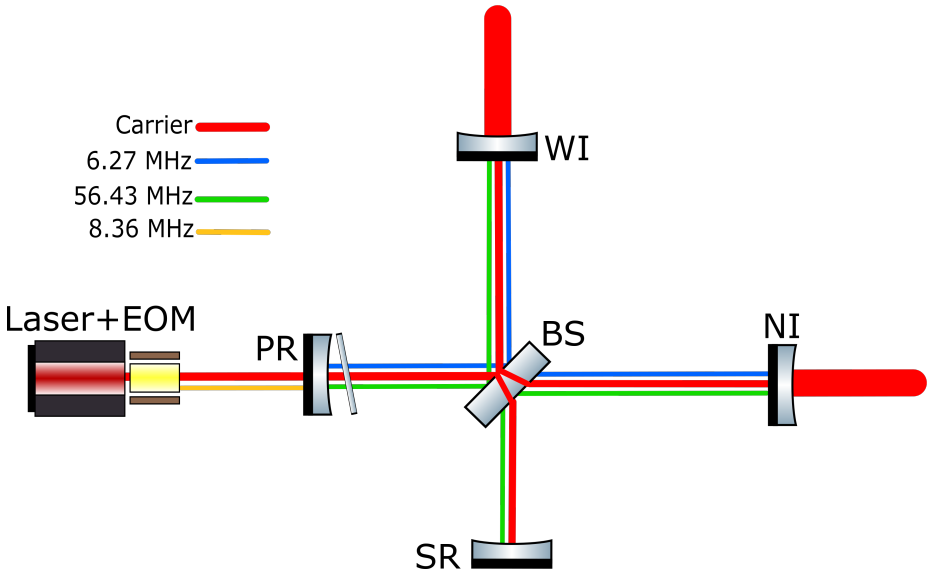

Figure 2: Representation of the resonance condition of the sidebands at the modulation frequencies in the CITF. f1 (6 MHz) is resonant in the PRC, f2 (56 MHz) is resonant in both the PRC and the SRC, f3 (8 MHz) is not resonant anywhere.

The working point of the longitudinal DoFs in the CITF is defined as follows:

- **PRCL:** zero-crossing of B2_6MHz_p, confronted with the maximum of the B2_6MHz upper and lower SBs. Without the arm cavities locked, the carrier is not resonant in the CITF and it does not show any evident peak while sweeping PRCL around its working point, so we take the SBs instead. Notice that upon reflection on the locked arm cavities, these SBs would gain an additional phase of 90°on reflection, so we add it manually to correctly pinpoint the working point of PRCL.
- **SRCL:** zero-crossing of B2_56MHz_p, confronted with the crossing point of the B2_56MHz upper and lower SBs.
- **MICH:** zero-crossing of B2_56MHz_q (the demodulation phase is chosen to maximize the **p** component with respect to the **q**, favouring the error signals for SRCL), confronted with the minimum of B1p.

In AdV+ the arm cavities will be aligned on the green laser, whose commissioning is underway at the time of writing. Therefore, the ITMs will be used as reference for alignment, meaning that, when a misalignment is detected for them via an error signal, the correction will be to translate the PR and tilt the BS to align the beam to the ITMs, rather than vice-versa.

2.2 Pykat lock routine

The simulation tool used for this work is `Pykat`[1] `v1.2.69`. In particular, A.Freise, one of Pykat main developers, prepared a python script that implements a lock and draglock routine. At the time of this note, this script is still in development and can be pulled from GitHub[2].
For this work, said routine has been modified quite heavily by removing many functions, unnecessary for the scope of this note. After doing this, we are left with a script that works as follows:

- `load the configuration file:` a configuration file (`avirgoplus_design1.kat`) is loaded. This configuration file is written following a specific convention for Pykat, that allows to automatically perform certain actions, like sweeping a DoF. In particular, every DoF is automatically defined by Pykat as one or more components, of which some parameter is changed following a certain rule and this variation is monitored by the power at a certain node of the ITF. For this step, the original algorithm has been modified by adding an option to only consider the CITF, which requires to change the error signals used to lock the longitudinal DoFs involved.
- `cavity pretuning:` to speed up the lock procedure, the longitudinal DoFs of the interferometer are brought in their nominal working point by sweeping them and using the DC power computed at the following points:
  - **PRCL:** maximum power at the symmetric port of the beam splitter. It is equal to the DC power of B4 if multiplied by the reflectivity of the pick-off plate. The script is still considering the complete ITF at this stage, so, despite the different definition, the working point found for PRCL is close enough to the correct one for the CITF.
  - **SRCL:** minimum power transmitted through the OMCs. Equal to B1.
  - **MICH:** minimum power transmitted through the OMCs. Equal to B1.

  These working point are defined in the `advplus.py` library.
- `check error signals:` the RF error signals for the longitudinal DoFs are displayed and their demodulation phase is tuned. Since we have set to work with the CITF, the signals used are `B2_6MHz_p` for PRCL, `B2_56MHz_p` for SRCL, `B2_56MHz_q` for MICH. Since SRCL and MICH use the same photodiode, its demodulation phase is chosen to maximize the `p`.
- `lock the CITF:` the CITF is locked in its working point. The script automatically computes the lock gains, but the user can scale them with custom factors. The user can also set the lock tolerance (measured in metres). The lock is displayed as the distance between the default position and the new working point, and the variation of the error signals along the sweep, that needs to remain inside the set tolerance for the lock to be successful. Assuming no interruption, every steps up to this point only needs to be performed once.
- `draglock:` the user has to select a component and its parameters to sweep (for example `PR` and `phi` would change the phase accumulated by the beam upon reflection on the PR, i.e. the PR is moving longitudinally). The CITF is kept locked accordingly to the set tolerances (if possible) during the sweep of this parameter. The draglock always starts from the working point, and finishes at a user selected extreme after the desired number of steps. Any number of detectors can be added to the CITF during this step, to obtain the needed sensing.
- `Create/merge tranches:` since the draglock always starts from the working point with null misalignment for each mirror, to simulate the error signals one needs to divide the sweep in two halves, both of them starting from 0 and reaching maximum absolute misalignment. The simulated data are saved on two distinct files as matrices, the one containing the data for the negative half of the sweep being inverted top-bottom beforehand, so that the two files can be merged into one containing the full sweep from the negative extreme to the positive extreme. Notice that by doing so the working point appears twice, so one of the two instances is deleted.

3 Draglock evaluation

Let us discuss a few details of the simulation. First of all, there is a soft constraint on the width of the tilt that is possible to consider.

3.1 The HOMs convergence

When a mirror is misaligned, assuming a small misalignment θ, the beam can be expressed in a succession of Hermite-Gauss polynomials weighted by increasing powers of θ ([3]). Therefore, for small θ, the modes of higher order than 01 and 10, can be negliected, but this hypothesis becomes less and less accurate as one reaches larger misalignment for the mirror of a cavity. Therefore, truncating the Hermite-Gauss polynomials expansion too soon might cause some non-negligible order to be ignored in the computation.
This is particularly relevant for a marginally stable cavity, as the ones in the CITF, since the HOMs generated in such a cavity are closer together than for a stable one, to the point where they actually enter the cavity's linewidth and be at least partially recycled in it. Therefore by neglecting these HOMs in the computation we can cause a portion of the beam power to "disappear", and the simulated alignment error signals becomes less representative of the reality the more significant this power loss is.
For this reason we first need to make sure that the simulated signals have "converged", meaning that, given the maximum misalignment of a given mirror, any mode of higher order than we are accounting for does not contribute to the simulated signals, but each additional HOM approximately doubles the computation time. We then need to strike the balance between the width of the misalignment and the computational time required for each mirror.
We found that, for a misalignment of $(-0.12; 0.12)\mu$rad, the simulated signals converge at the 10th order of modes, which translated to around eight hours of computational time for each of the eight tranches of the simulation. This is considered to be a sufficient balance between exploring the widest possible sweep for each misalignment and keeping the computational time reasonable for this task.
Another important aspect is given by the lock of the longitudinal DoFs, for which the set tolerances are:

- `PRCL`: lock tolerance: $5 \cdot 10^{-17}$ m $\Rightarrow 6.8845 \cdot 10^{-10}$ W
- `MICH`: lock tolerance: $5 \cdot 10^{-14}$ m $\Rightarrow 1.2286 \cdot 10^{-8}$ W
- `SRCL`: lock tolerance: $5 \cdot 10^{-17}$ m $\Rightarrow 6.2956 \cdot 10^{-12}$ W

We can proceed now by showing the lock result for the misalignment of each mirror of the CITF.

3.2 Power Recycling

Let us begin by misaligning the PR mirror. By tilting it from -0.12μrad to 0.12μrad, we obtain the following plot for the longitudinal error signals:

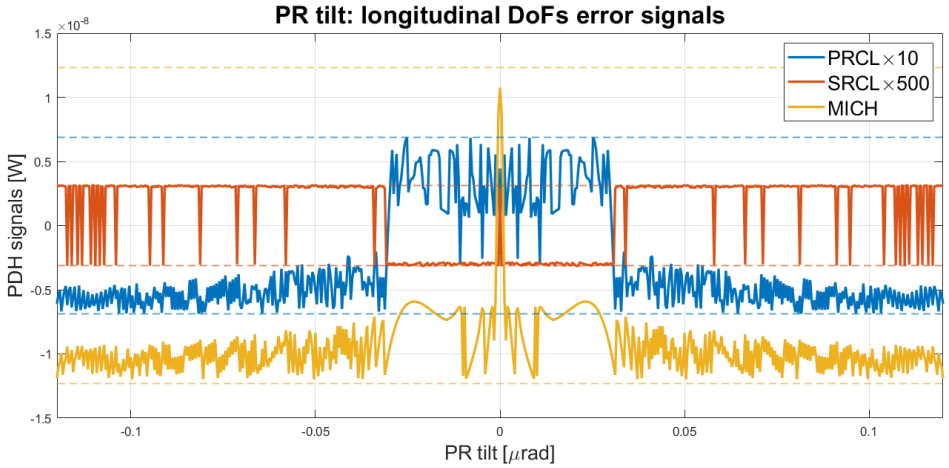

Figure 3: Longitudinal error signals plotted while tilting the PR mirror. PRCL and SRCL signals are magnified for visual clarity. The dashed lines represent the lock tolerances per each DoF, with the same colours as shown in the legend.

The error signals graze the set tolerance threshold, but never cross it. Let us look at the sideband to evaluate their behaviour. The 6MHz is resonant in the PRC of the CITF, while the carrier is not. For this reason, engaging the lock or not does not produce a significant enough difference in the PRC length to notice any difference on the carrier field, but disturbing the resonance condition for the sidebands may cause them to change significantly:

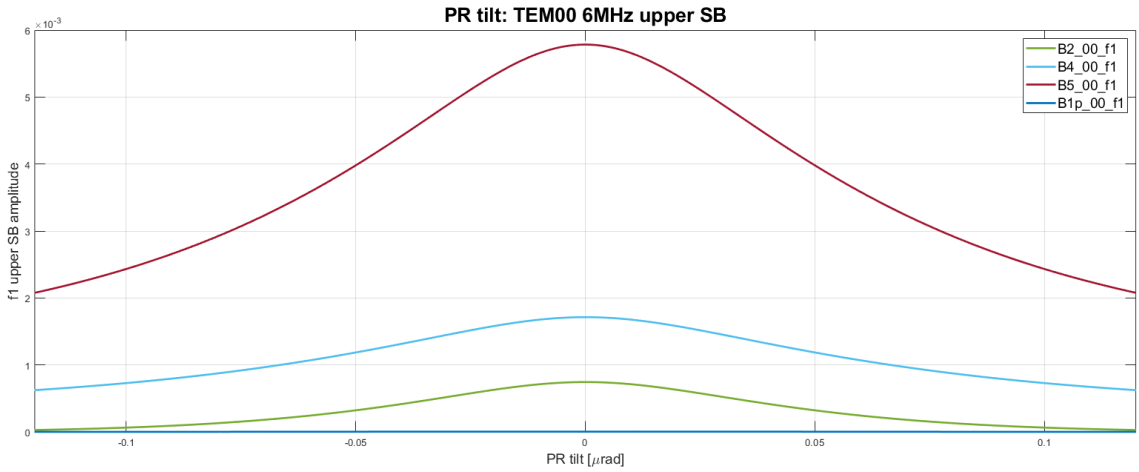

Figure 4: Amplitude variation of the TEM00_f1 channels for the CITF, while tilting the PR mirror.

And finally, the following plot shows the change in the working point of each DoF:

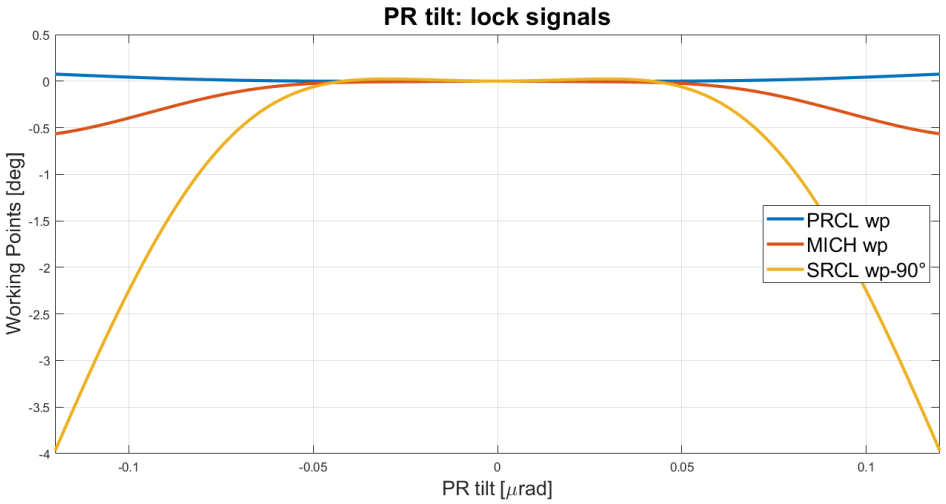

Figure 5: Change of working point of the longitudinal DoFs while tilting the PR mirror, expressed as the phase accumulated by the beam upon reflection on each mirror (PR for PRCL, SR for SRCL, WI and NI with opposite sign for MICH).

As a reference, let us show the behaviour of the 6MHz upper sideband with and without the lock routine for the same tilt of the PR.

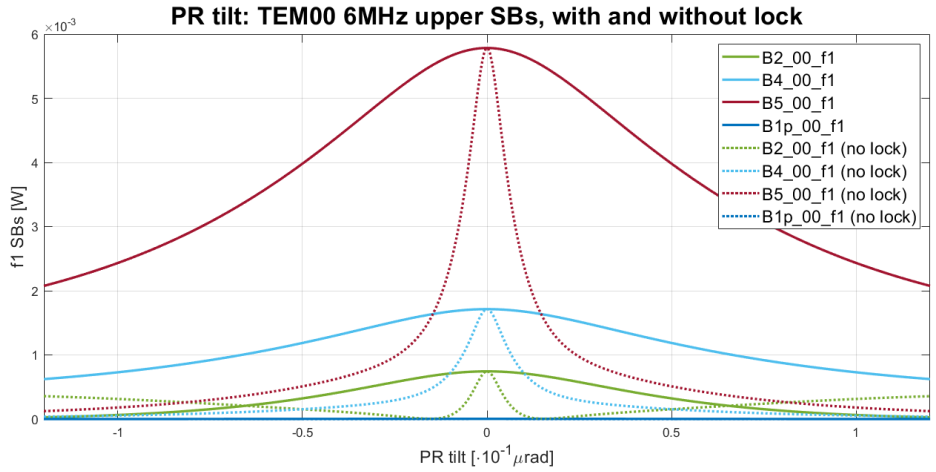

Figure 6: Amplitude variation of the TEM00_f1 channels for the CITF while misaligning the PR. Comparison of the locked CITF (full lines) with the case where the cavities are kept free (dotted lines).

The f1 upper sideband change more abruptly when the lock routine is not implemented.
We can conclude that the lock routine worked as it was supposed to. It kept the error signals inside the tolerances and prevented the 6MHz sideband to change as quickly as it would have without applying the routine. We are now confident in the good behaviour of this procedure, and we will quickly show the results for the other mirrors without repeating this test.

3.3 Signal Recycling

Let us show the same plots for the misalignment of the SR mirror.

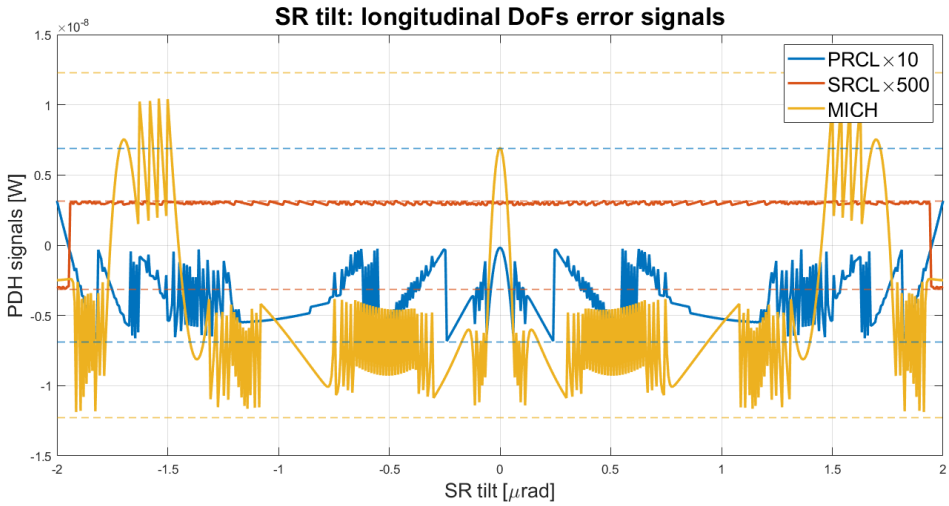

Figure 7: Longitudinal error signals plotted while tilting the SR mirror. PRCL and SRCL signals are magnified for visual clarity. The dashed lines represent the lock tolerances per each DoF, with the same colours as shown in the legend.

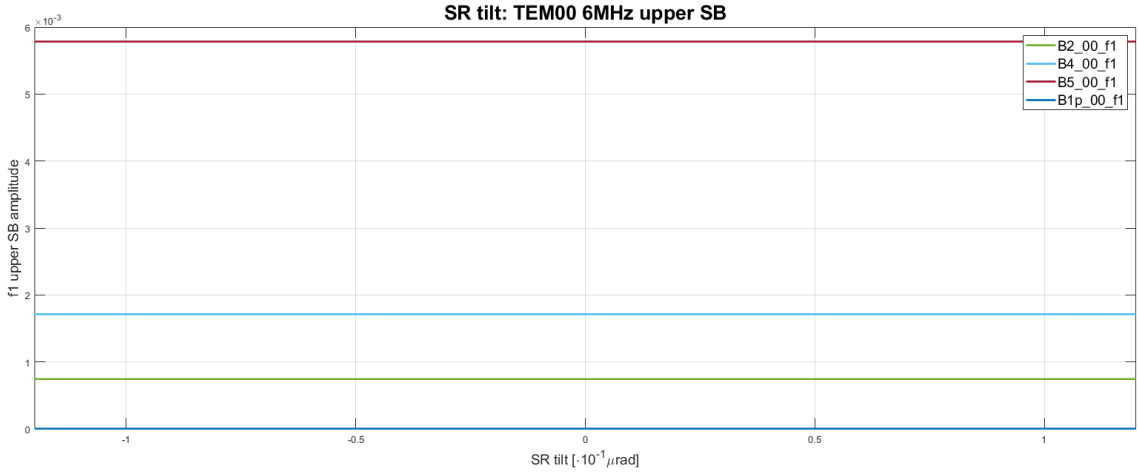

Figure 8: Amplitude variation of the TEM00_f1 channels for the CITF, while tilting the SR mirror.

And finally, the following plot shows the change in the working point of each DoF:

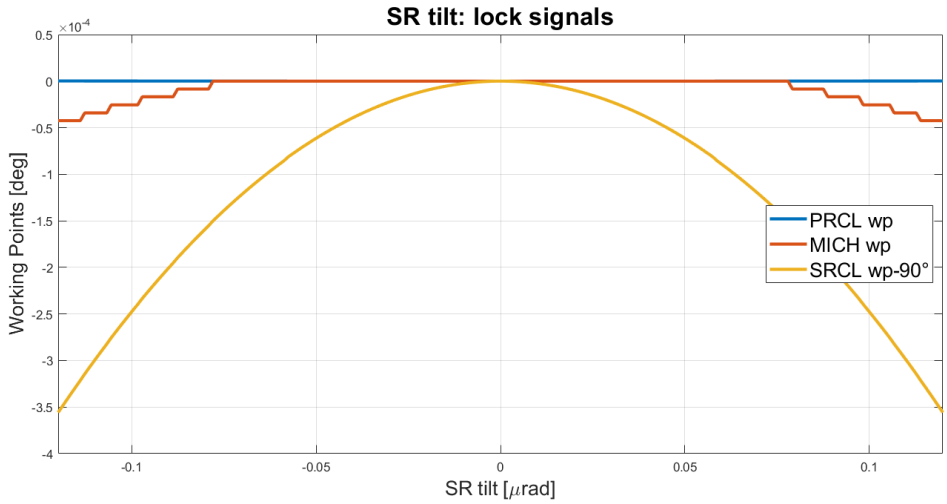

Figure 9: Change of working point of the longitudinal DoFs while tilting the SR mirror, expressed as the phase accumulated by the beam upon reflection on each mirror (PR for PRCL, SR for SRCL, WI and NI with opposite sign for MICH).

We can conclude that the routine was able to keep the CITF locked while misaligning the SR.

3.4 West Input

Let us show the same plots for the misalignment of the WI mirror.

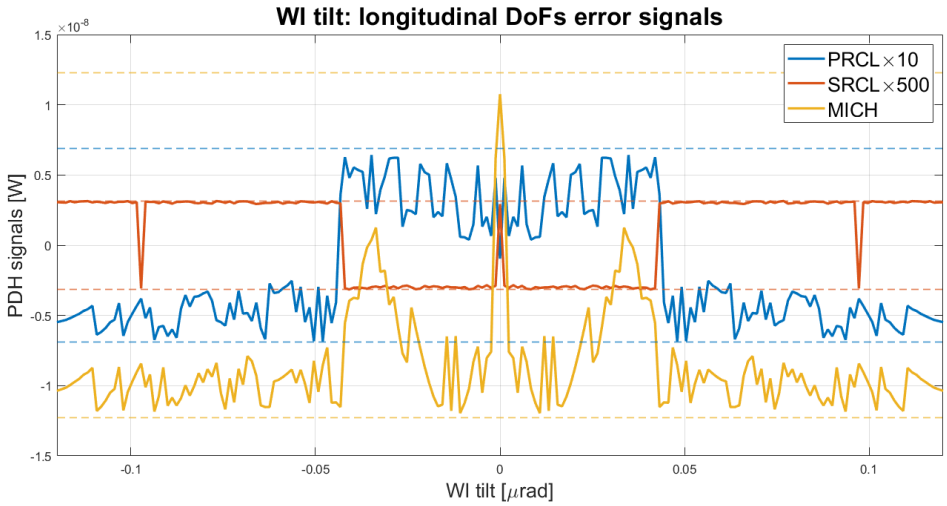

Figure 10: Longitudinal error signals plotted while tilting the WI mirror. PRCL and SRCL signals are magnified for visual clarity. The dashed lines represent the lock tolerances per each DoF, with the same colours as shown in the legend.

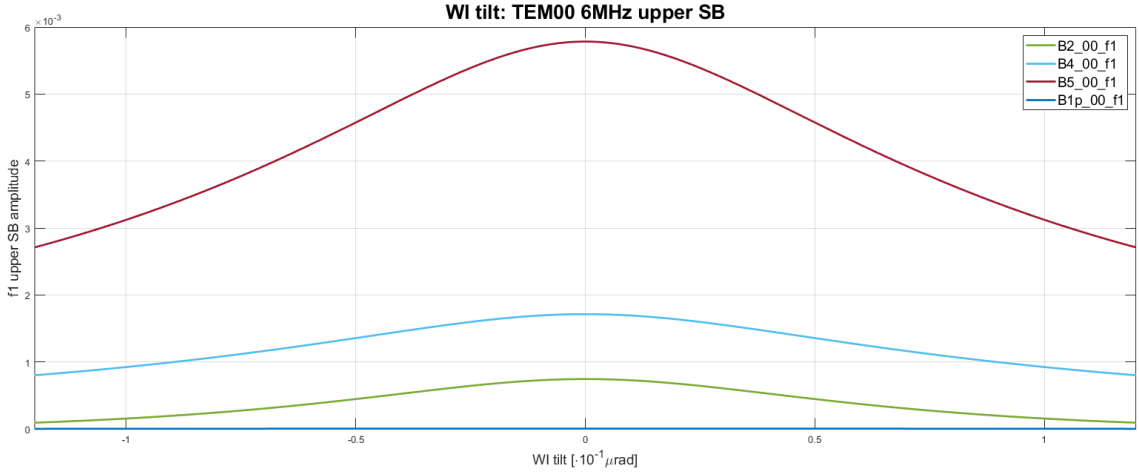

Figure 11: Amplitude variation of the TEM00_f1 channels for the CITF, while tilting the WI mirror.

And finally, the following plot shows the change in the working point of each DoF:

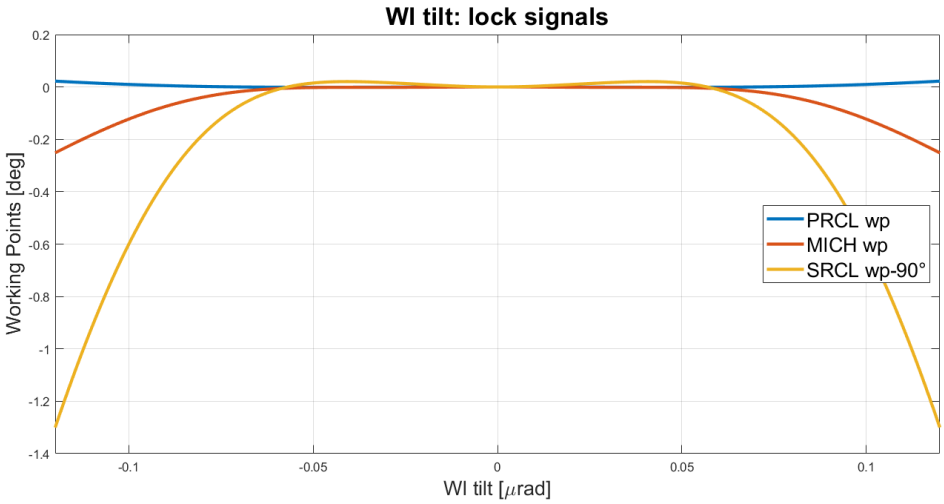

Figure 12: Change of working point of the longitudinal DoFs while tilting the WI mirror, expressed as the phase accumulated by the beam upon reflection on each mirror (PR for PRCL, SR for SRCL, WI and NI with opposite sign for MICH).

We can conclude that the routine was able to keep the CITF locked while misaligning the WI.

3.5 North Input

Let us show the same plots for the misalignment of the WI mirror.

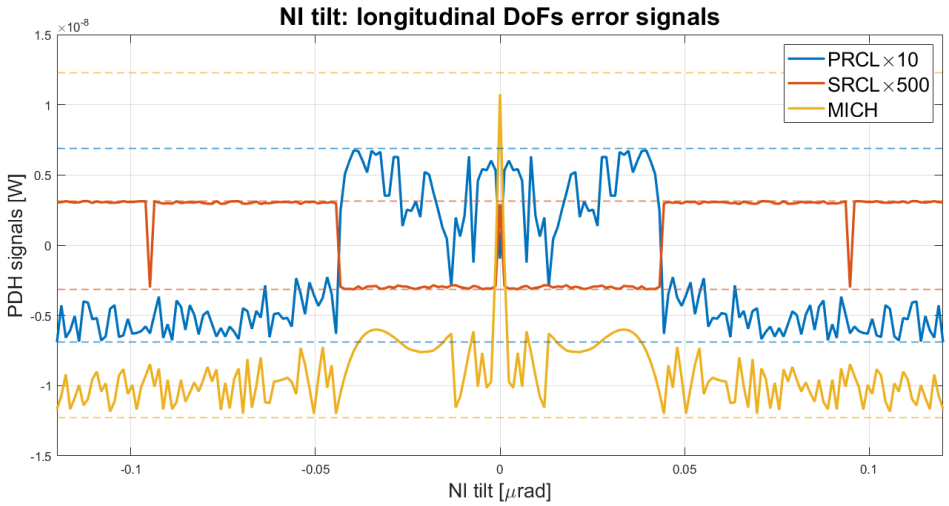

Figure 13: Longitudinal error signals plotted while tilting the NI mirror. PRCL and SRCL signals are magnified for visual clarity. The dashed lines represent the lock tolerances per each DoF, with the same colours as shown in the legend.

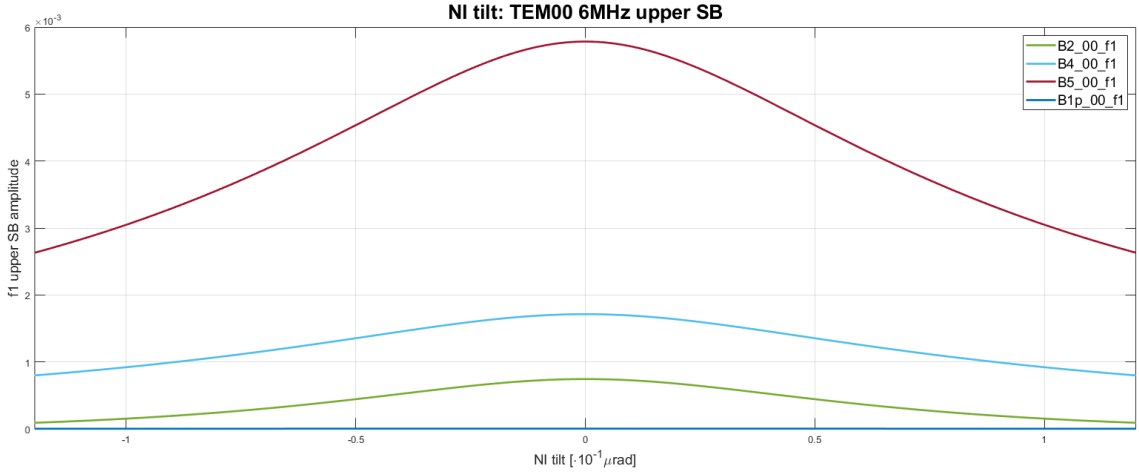

Figure 14: Amplitude variation of the TEM00_f1 channels for the CITF, while tilting the NI mirror.

And finally, the following plot shows the change in the working point of each DoF:

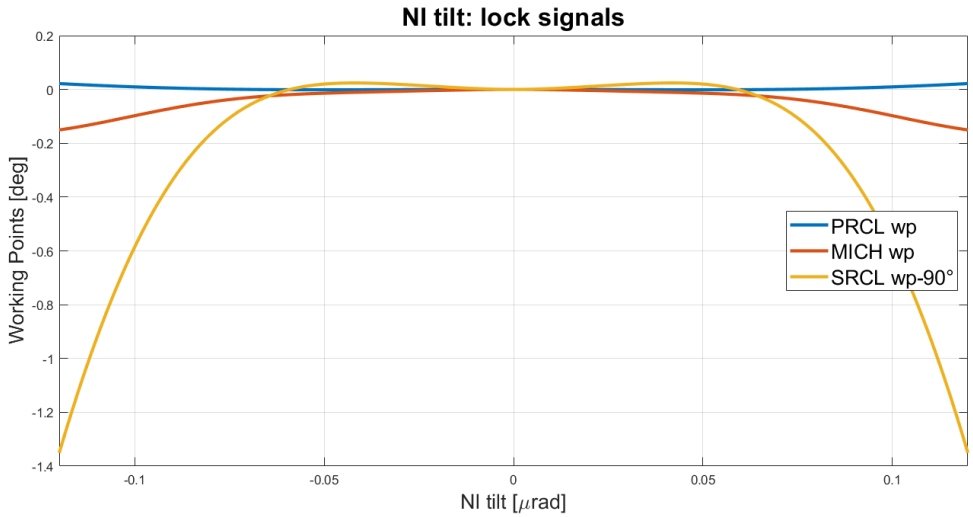

Figure 15: Change of working point of the longitudinal DoFs while tilting the NI mirror, expressed as the phase accumulated by the beam upon reflection on each mirror (PR for PRCL, SR for SRCL, WI and NI with opposite sign for MICH).

We can conclude that the routine was able to keep the CITF locked while misaligning the NI.

4 QPDs signals

To build the alignment error signals we use the Ward technique with the addition of the DC channels. Let us briefly discuss the Ward technique.

4.1 Ward technique

Let us consider a resonant cavity for which we want to obtain an alignment error signal. To do so, we can apply a phase modulation to the laser beam resonating in the cavity that, if appropriately chosen, can function as a phase reference that gives the error signal. Let us see in details how this works.
A misaligned cavity causes the beam stored inside to change its optical path to a combination of a shift and a tilt with respect to the original optical path. This produces a scattering of the beam power to higher order modes, weighted by growing powers of the beam tilt and/or shift. By truncating this expansion at first order, we can write the expression of the beam inside the cavity as follows:

$$E = \psi_0 U_0 e^{i\omega t} + \xi e^{i(\alpha+\Phi(z))}\psi_1 U_1 e^{i(\omega+\delta\omega)t} \tag{4.1}$$

where the U_n are the Hermite-Gauss polynomials of the expansion, each with amplitude ψ_n, ω is the carrier field angular frequency, and the first order mode has a frequency shift $\delta\omega$ and an accumulated dephasing $\Phi(z)$ with respect to the 00 mode. With an appropriate choice of ξ and α we can obtain the desired combination of tilt and shift. For example, a pure beam tilt by a small angle θ_b is given by:

$$\alpha = \frac{\pi}{2} \qquad \xi = \frac{k w_0}{\sqrt{2\pi}}\theta_b \tag{4.2}$$

where w_0 is the beam waist size. This results in [4]:

$$E = \psi_0 U_0 e^{i\omega t} + i\frac{k w_0}{\sqrt{2\pi}}\theta_b \psi_1 U_1 e^{i(\omega+\delta\omega)t+\Phi(z)}$$

while a pure beam shift by a small δ_b is given by:

$$\alpha = 0 \qquad \xi = \sqrt{\frac{2}{\pi}}\frac{\delta_b}{w_0} \tag{4.3}$$

which results in [4]:

$$E = \psi_0 U_0 e^{i\omega t} + \sqrt{\frac{2}{\pi}}\frac{\delta_b}{w_0}\psi_1 U_1 e^{i(\omega+\delta\omega)t+\Phi(z)}$$

Notice that we take a ξ proportional to both θ_b and δ_b, always assumed small.
Let us consider a beam like the one represented in (4.1) to which we add a phase modulation at frequency Ω. The laser field can be expanded in Bessel polynomials representing the carrier field and its sidebands at $\omega \pm \Omega$ frequencies, which are reflected by the cavity with a reflectivity that depends on their frequency:

$$\begin{aligned} E_{ref} = {} & \psi_0 \left[R_0 J_0 + iR_+ J_1 e^{i\Omega t} + iR_- J_1 e^{-i\Omega t}\right] U_0 e^{i\omega t} + \\ & + \psi_1 \left[R_0 J_0 + iR_+ J_1 e^{i\Omega t} + iR_- J_1 e^{-i\Omega t}\right] \xi e^{i(\alpha+\Phi(z))} U_1 e^{i(\omega+\delta\omega)t} \end{aligned} \tag{4.4}$$

We assume $\delta\omega$ to be small enough that the reflectivity of the cavity does not change significantly between zero order and first order Hermite-Gauss modes. By detecting the reflected beam with a photodiode, we would measure its power given by the square of (4.4):

$$\begin{aligned} P = |E_{ref}|^2 = {} & \left[|\psi_0|^2 U_0^2 + \psi_0\psi_1^* U_0 U_1 e^{-i\delta\omega t}\xi e^{-i(\alpha+\Phi(z))} + \psi_0^*\psi_1 U_0 U_1 e^{i\delta\omega t}\xi e^{i(\alpha+\Phi(z))} + o(\xi)\right] \cdot \\ & \cdot \left\{\left[|R_0|^2 J_0^2 + |R_+|^2 J_1^2 + |R_-|^2 J_1^2\right] + \right. \\ & + iJ_0 J_1 \left[\left(R_0^* R_+ - R_0 R_-^*\right) e^{i\Omega t} + \left(R_0^* R_- - R_0 R_+^*\right) e^{-i\Omega t}\right] + \\ & \left. + J_1^2 \left[R_+ R_-^* e^{i2\Omega t} + R_+ R_-^* e^{-i2\Omega t}\right]\right\} \end{aligned} \tag{4.5}$$

where we have grouped the contributions by their order in Ω. We can now demodulate by multiplying by another signal:

$$s(t) = \frac{1}{2}\left(e^{i\Omega t} + e^{-i\Omega t}\right) e^{i\phi}$$

where ϕ is the demodulation phase. By doing so, the terms in (4.5) with frequency Ω become DC and the frequency of all the others becomes Ω, 2Ω exc. By low-passing them we can discard them all and only keep the new DC contribution, with the demodulation phase as a new degree of freedom. So far the process is identical to the PDH technique for longitudinal control, except that the coefficient in the first line of (4.5) contains additional terms with the beating between TEM00 and TEM01/TEM10.
The power detected by a real photodiode is the integral of (4.5) over the photodiode surface, that can be assumed to be infinite with respect to the beam size. However, by computing the integral we make the information about the misalignment disappear, because the U_n are orthogonal functions. We can solve this problem by splitting the photodiodes in two halves and taking the difference of their detected power:

$$P = \int_{-\infty}^{+\infty} EE^* ds \rightarrow \int_{-\infty}^{0} EE^* ds - \int_{0}^{\infty} EE^* ds$$

by doing so we only select the odd contributions in the surviving term of (4.5). At the end, the only remaining contribution to be integrated is:

$$\begin{aligned} P \cdot s(t) = &\left[\psi_0 \psi_1^* U_0 U_1 e^{-i\delta\omega t} \xi e^{-i(\alpha+\Phi(z))} + \psi_0^* \psi_1 U_0 U_1 e^{i\delta\omega t} \xi e^{i(\alpha+\Phi(z))}\right] \cdot \\ &\cdot i J_0 J_1 \left[\left(R_0^* R_+ - R_0 R_-^*\right) e^{i\Omega t} + \left(R_0^* R_- - R_0 R_+^*\right) e^{-i\Omega t}\right] \end{aligned} \tag{4.6}$$

By taking the imaginary component and computing the integral we are left with the following:

$$P \propto 2 U_0 U_1 \xi \sin\left(\alpha - \Phi(z)\right) \tag{4.7}$$

Hidden in the $\propto$ sign there is the same coefficient that gives the shape to the PDH signals, but we are mostly interested in the interaction between U_0 and U_1. From (4.7) we notice that the phase accumulated by the beam in the optical path matters. A split photodiode set in a point where $\Phi(z) = 0$ would detect the signal of maximum intensity when $\alpha = \pi/2$, which corresponds to the pure tilt of the beam. Conversely, a split photodiode set in a point where $\Phi(z) = \pi/2$ would see the signal of maximum intensity when $\alpha = 0$, which corresponds to the pure shift of the beam.
By taking quadrant photodiodes we ensure maximum sensitivity of the sensors to tilt and shift of the beam in both transverse directions.

4.2 Far-field, near-field and Gouy phase.

Let us discuss how many photodiodes are we going to implement and why.
By tuning the Gouy phase of the beam impinging on the QPD, it is possible to obtain a laser field with either spheric waves ($\phi_G = 90$) or plane waves ($\phi_G = 0$), that correspond to near and far field approximation respectively. When a mirror tilts, it produces a displacement of the beam in the corresponding cavity that is a linear combination of a tilt and a shift of the optical axis with respect of the line that passes through the vertices of the mirrors:

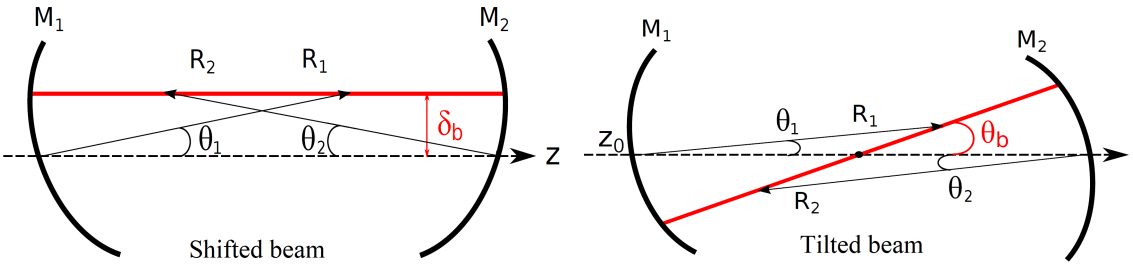

Figure 16: Diagram of a cavity with tilted mirrors in such a way to produce a pure shift (left) and a pure tilt (right) of the laser beam.[5]

One can tune the Gouy phase of the beam by using a telescope, but in Finesse it is sufficient to specify that, when the beam passes through a space, it needs to acquire a specific Gouy phase.

In the near-field or far-field approximation, a laser beam is only affected by a tilt and a shift respectively:

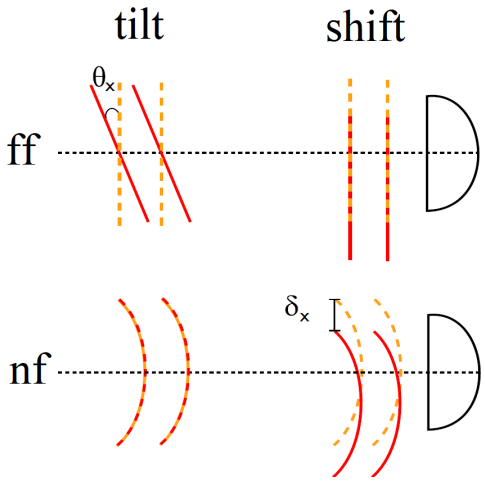

Figure 17: Diagram of the effect of the tilt or of the shift on a beam in the far field and near field approximation. The far field is not sensitive to the shift, while the near field is not sensitive to the tilt.[5]

From this we understand that each channel needs one QPDs each for the near-field and far-field approximations. Furthermore, for the CITF we have four detectors (B2, B4, B5, B1p) and three modulation frequencies (**f1** = 6 MHz, **f2** = 56 MHz, **f3** = 8 MHz). Finally, like a PDH signal each of them has two quadratures, for a total of 48 signals. Additionally since, as it will be clear in the following section, the SR tilt is almost invisible on every RF alignment error signal in the CITF, we also considered the DC channels for the same photodiodes, that make for 8 additional signals.

4.3 Alignment error signals

The following is the collection of the alignment error signals shown for each DoF of the CITF, already phase tuned, plus the corresponding compass plot to show the coupling among them. As previously mentioned, the modulation frequencies are the following:

- **f1** = 6270777 Hz
- **f2** = 56436993 Hz
- **f3** = 8361036 Hz

In the following plots we present the **p** component of each alignment error signal with the corresponding demodulation phase already tuned to maximize its optical gain. The **q** component will also be shown, dotted, to prove that the tuning worked as intended.
To perform this phase tuning, we developed Matlab script that works following this logic:

- Since the alignment working point of each mirror is given, by definition, by a null misalignment, the minimum absolute value of each error signal indicate the working point. In particular, since, as we mentioned in Subsection 2.2, the draglock must always start from the working point, the minimum absolute value of the all the error signals is always zero, and it is always present in the discrete number of points that compose the simulated data.
- We consider the two points adjacent to the working point. These two points are the values taken by the imaginary part of the complex error signal for those specific values of the mirror misalignment. We compute the absolute value and the argument (which is the demodulation phase) of this complex number, and then compute the slope of the straight line that passes through this two points, knowing that in such a small interval, this line well represents the **p** component of the error signal.
- We can now increase step by step the argument of the complex error signal, take its imaginary component in the same two positions and compute again the slope of the straight line that passes through them. When the product between the slopes computed at the steps `k` and `k+1` is null or negative, than null slope has been crossed between these two steps and the current total increment of the demodulation phase gives the correct tuning. With small enough steps there is no need for further investigation. The script we used looks for the correct tuning with steps of 0.5°.

We also check the demodulation phase tuning externally, by choosing a few random signals among all the available ones, plotting their **p** component for all the demodulation phases between 0°and 180°in steps of 5°and confronted the phase of the one that appeared to have the maximum slope with the phase found by the script. For every signal checked, the script appeared to have worked as intended.
Notice that the optimal demodulation phase could theoretically be found by just computing $\phi = \arctan\left(-\frac{q}{p}\right)$. We have chosen to proceed in this way because it allows for a visual verification of the result, to both verify that the found demodulation phase is correct and that the resulting error signal is meaningful.

We now present the simulated alignment error signals and the corresponding compass plots:

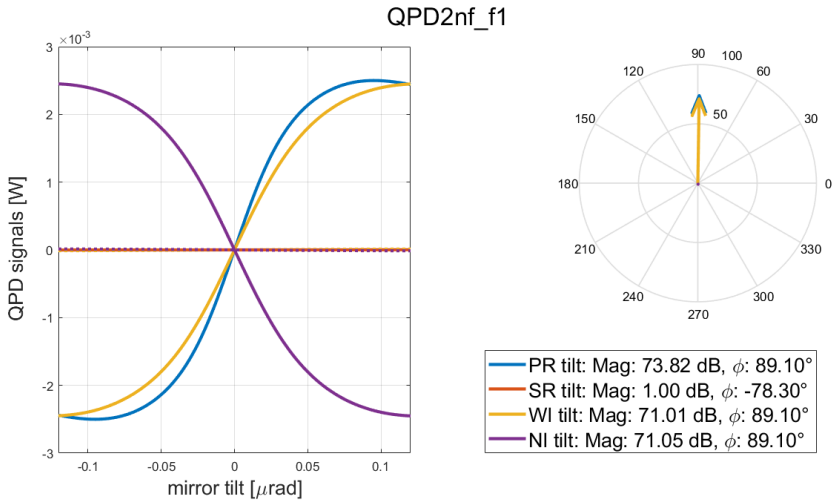

Figure 18: the simulated signals for QPD2nf_f1 with corresponding compass plot. Both components of the error signals are show (the quadrature components are dotted).

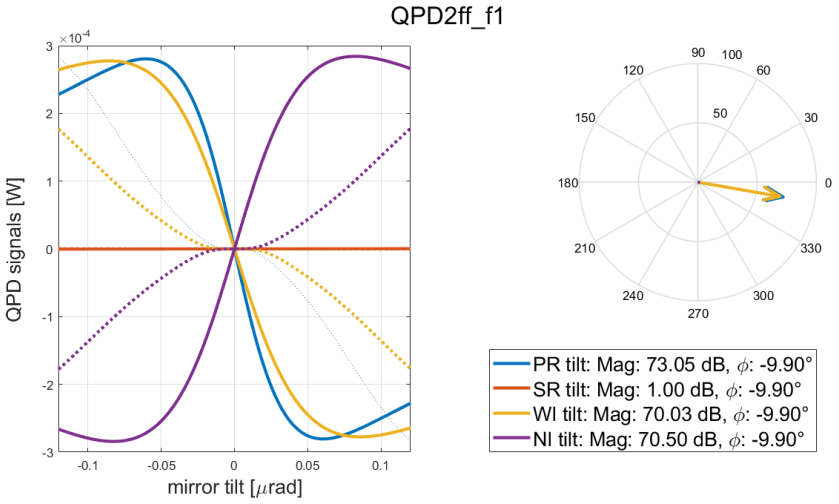

Figure 19: the simulated signals for QPD2ff_f1 with corresponding compass plot. Both components of the error signals are show (the quadrature components are dotted).

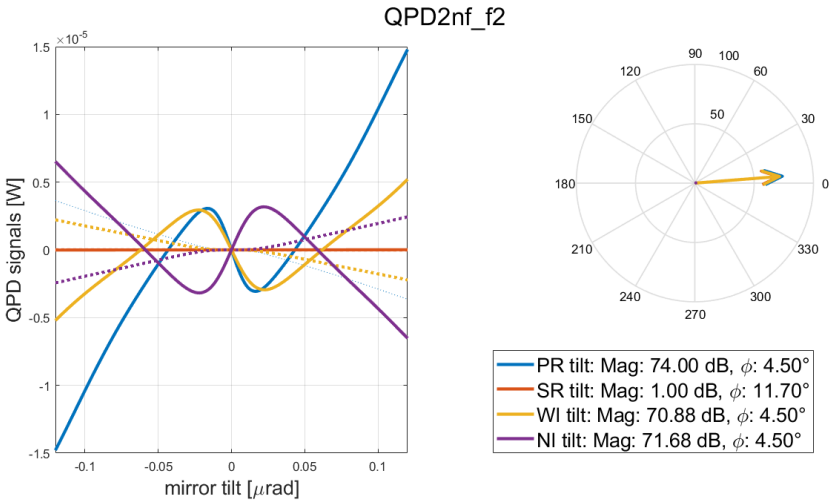

Figure 20: the simulated signals for QPD2nf_f2 with corresponding compass plot. Both components of the error signals are show (the quadrature components are dotted).

This is clearly a bad error signal: in the swept misalignment for each mirror, it appears to have multiple zero crossing and is therefore unusable for the sensing.

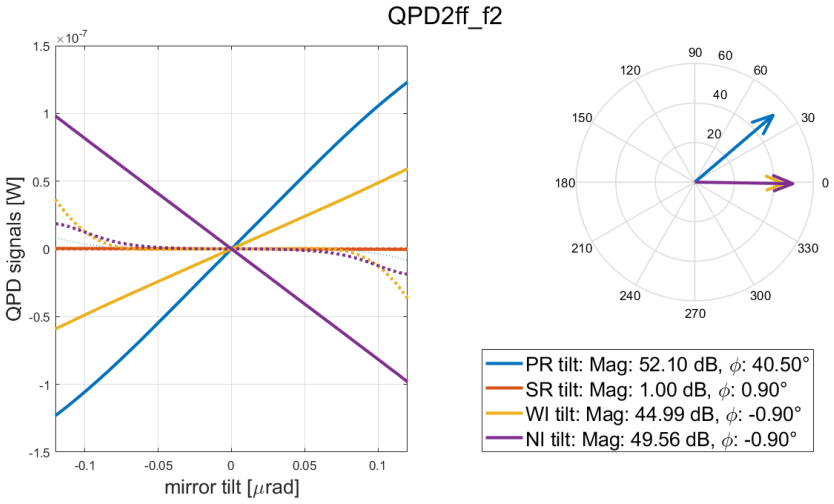

Figure 21: the simulated signals for QPD2ff_f2 with corresponding compass plot. Both components of the error signals are show (the quadrature components are dotted).

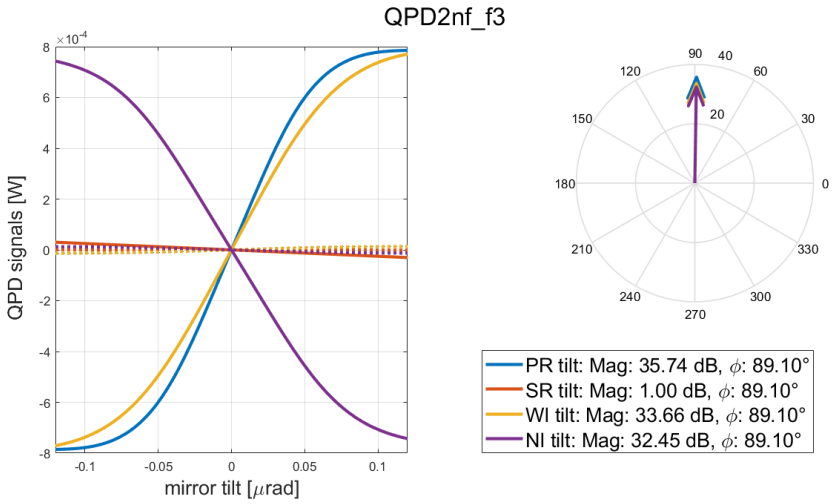

Figure 22: the simulated signals for QPD2nf_f3 with corresponding compass plot. Both components of the error signals are show (the quadrature components are dotted).

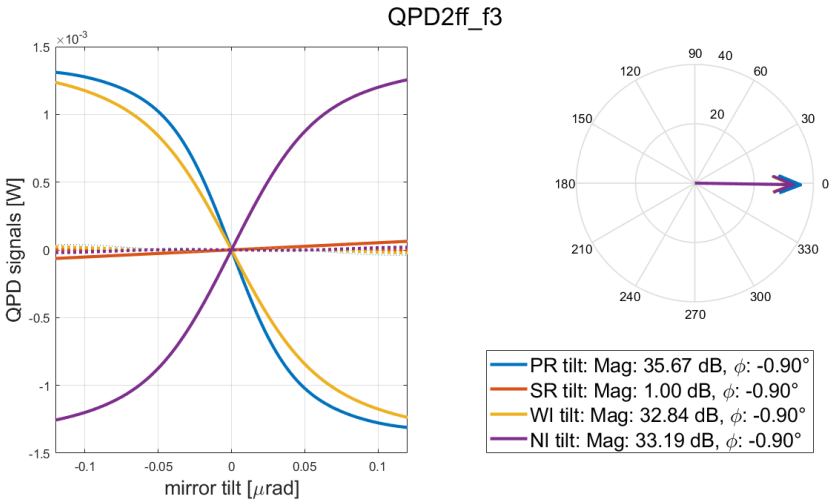

Figure 23: the simulated signals for QPD2ff_f3 with corresponding compass plot. Both components of the error signals are show (the quadrature components are dotted).

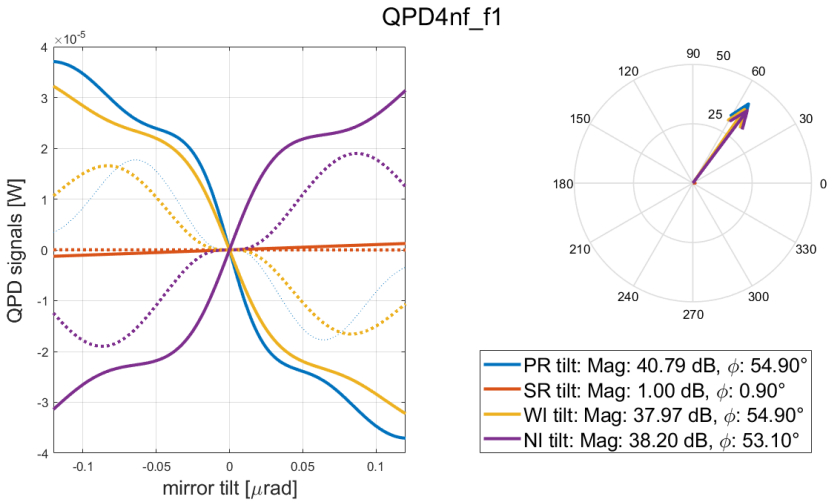

Figure 24: the simulated signals for QPD4nf_f1 with corresponding compass plot. Both components of the error signals are show (the quadrature components are dotted).

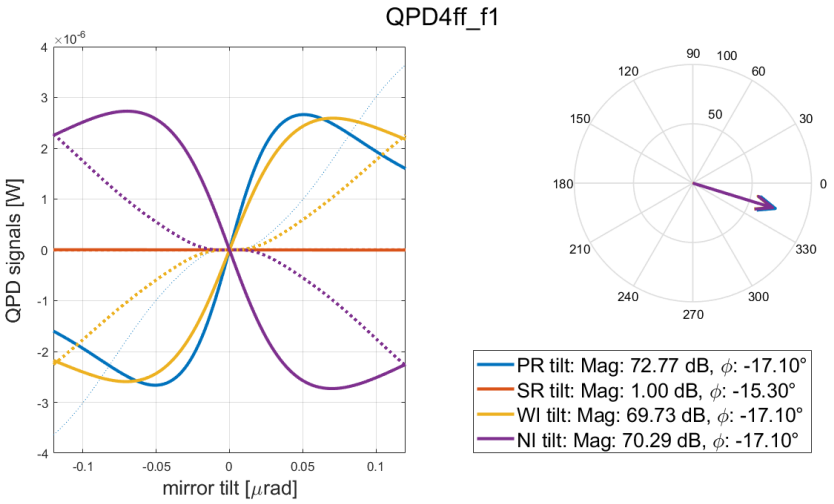

Figure 25: the simulated signals for QPD4ff_f1 with corresponding compass plot. Both components of the error signals are show (the quadrature components are dotted).

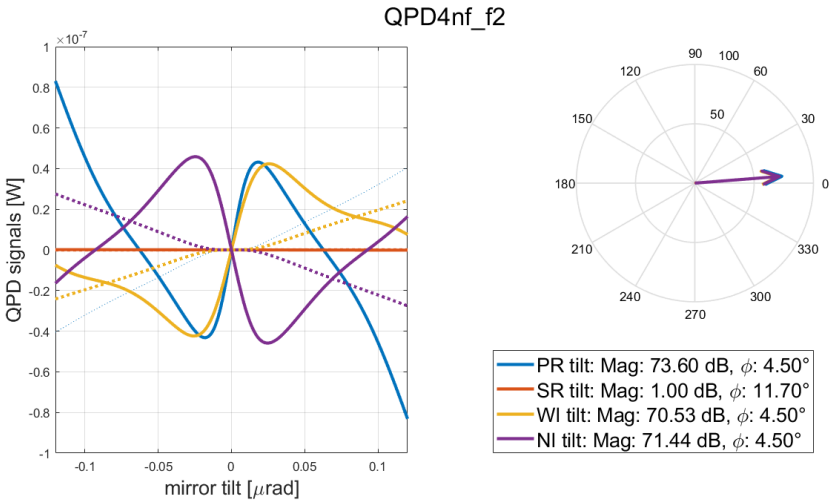

Figure 26: the simulated signals for QPD4nf_f2 with corresponding compass plot. Both components of the error signals are show (the quadrature components are dotted).

This is also a bad error signal, due to the multiple zero crossings in the swept misalignment.

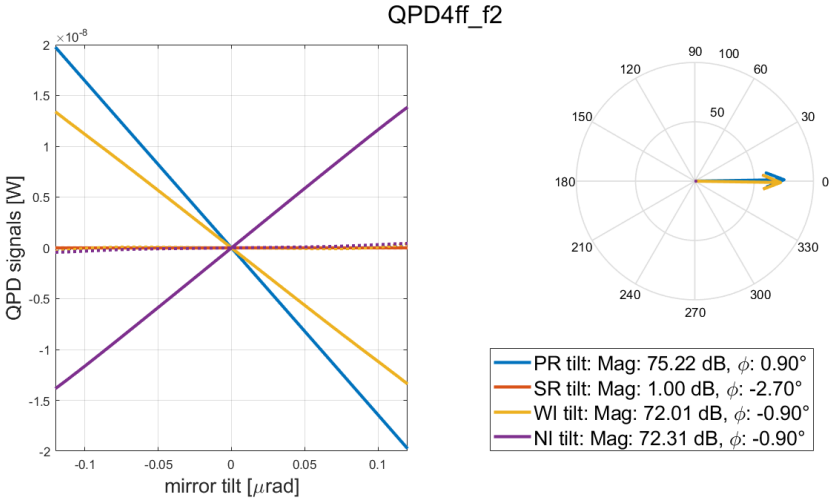

Figure 27: the simulated signals for QPD4ff_f2 with corresponding compass plot. Both components of the error signals are show (the quadrature components are dotted).

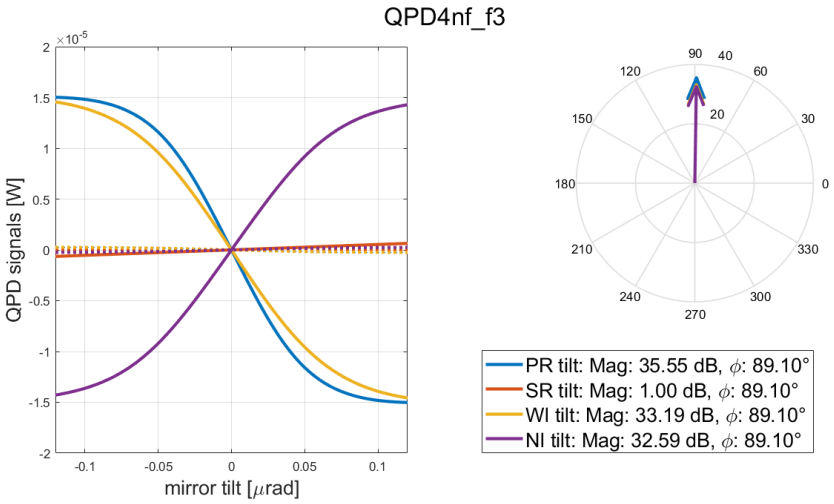

Figure 28: the simulated signals for QPD4nf_f3 with corresponding compass plot. Both components of the error signals are show (the quadrature components are dotted).

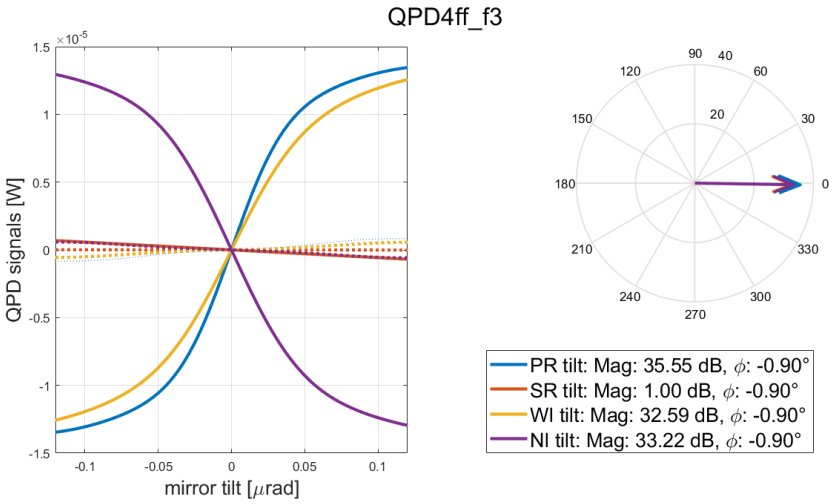

Figure 29: the simulated signals for QPD4ff_f3 with corresponding compass plot. Both components of the error signals are show (the quadrature components are dotted).

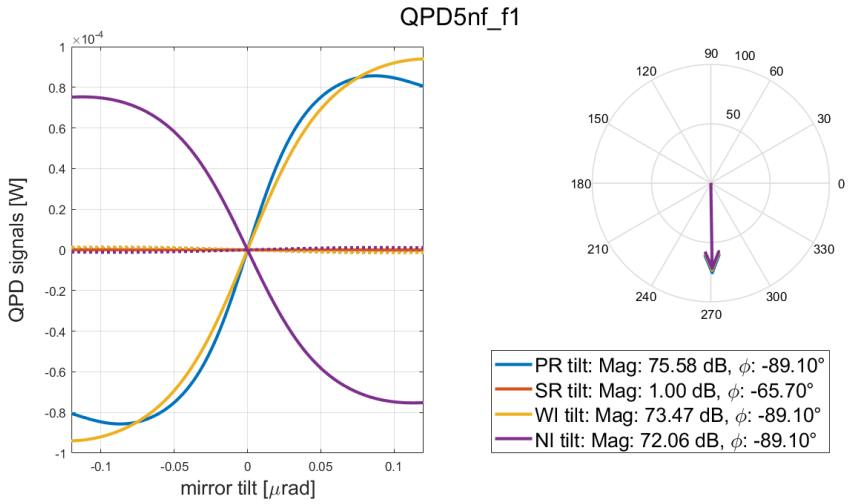

Figure 30: the simulated signals for QPD5nf_f1 with corresponding compass plot. Both components of the error signals are show (the quadrature components are dotted).

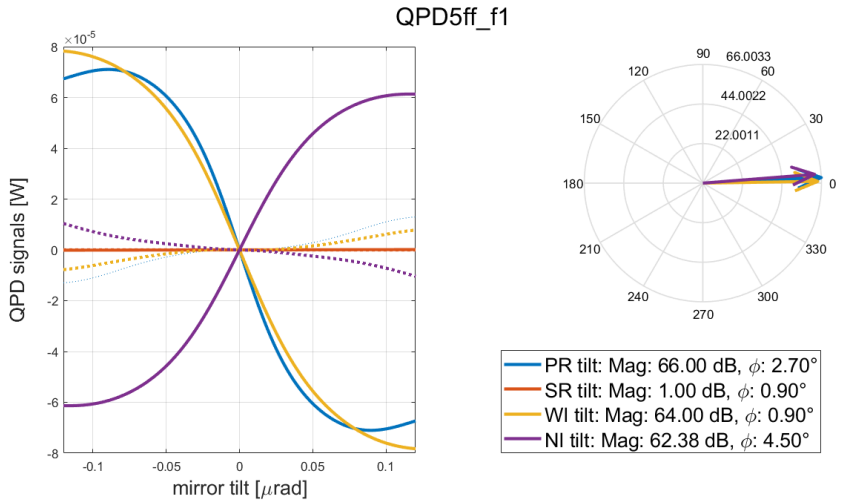

Figure 31: the simulated signals for QPD5ff_f1 with corresponding compass plot. Both components of the error signals are show (the quadrature components are dotted).

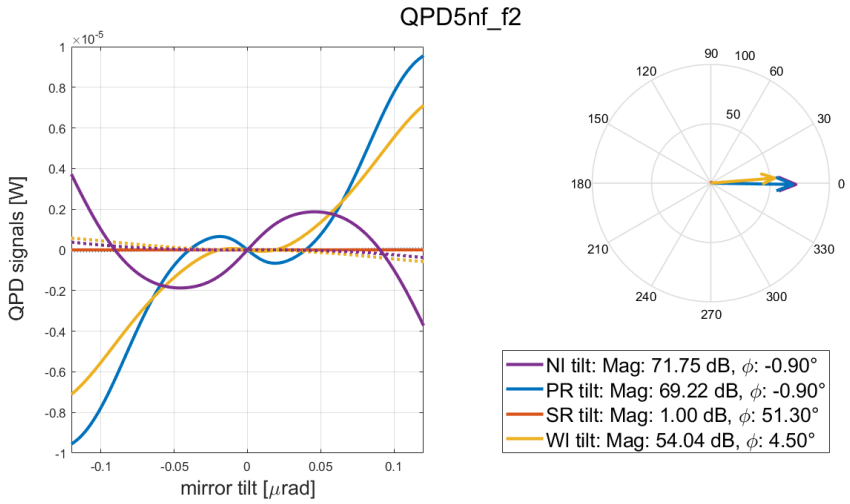

Figure 32: the simulated signals for QPD5nf_f2 with corresponding compass plot. Both components of the error signals are show (the quadrature components are dotted).

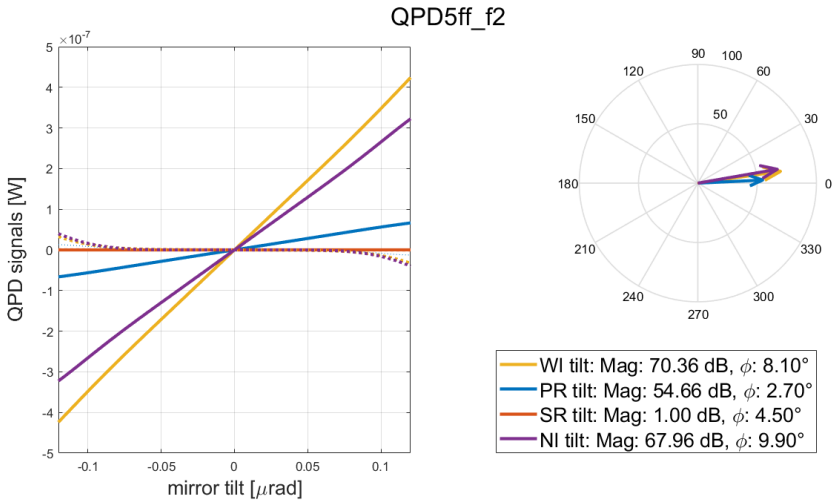

Figure 33: the simulated signals for QPD5ff_f2 with corresponding compass plot. Both components of the error signals are show (the quadrature components are dotted).

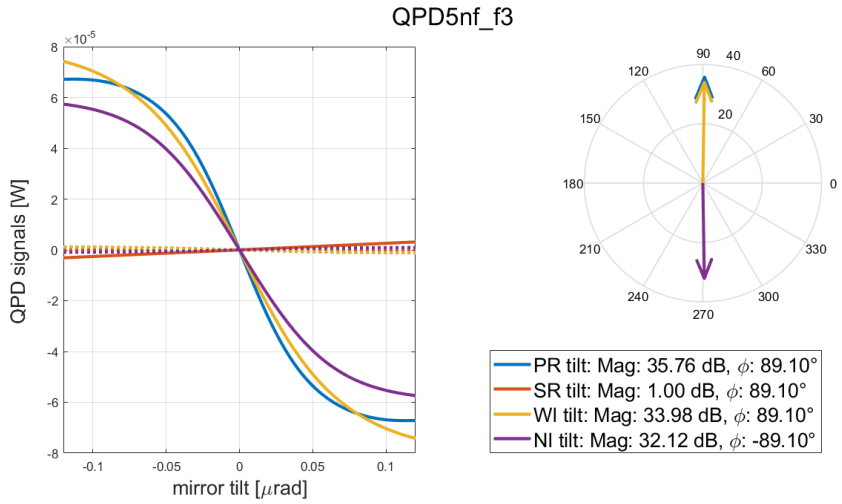

Figure 34: the simulated signals for QPD5nf_f3 with corresponding compass plot. Both components of the error signals are show (the quadrature components are dotted).

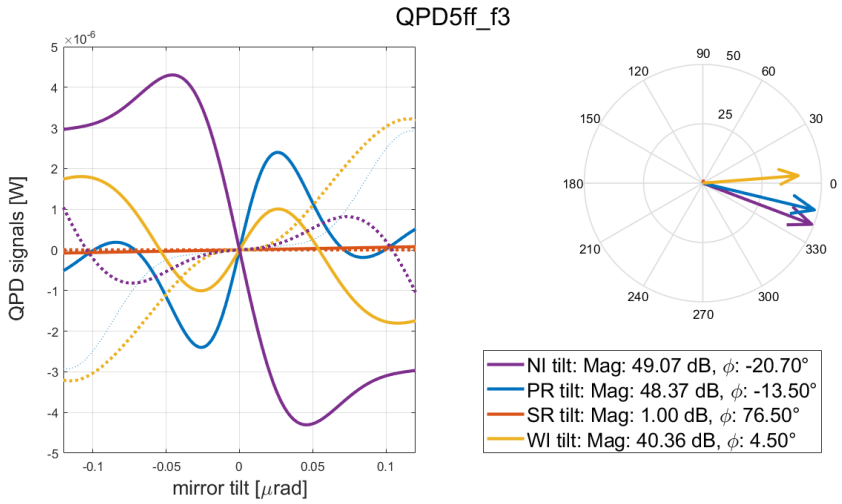

Figure 35: the simulated signals for QPD5ff_f3 with corresponding compass plot. Both components of the error signals are show (the quadrature components are dotted).

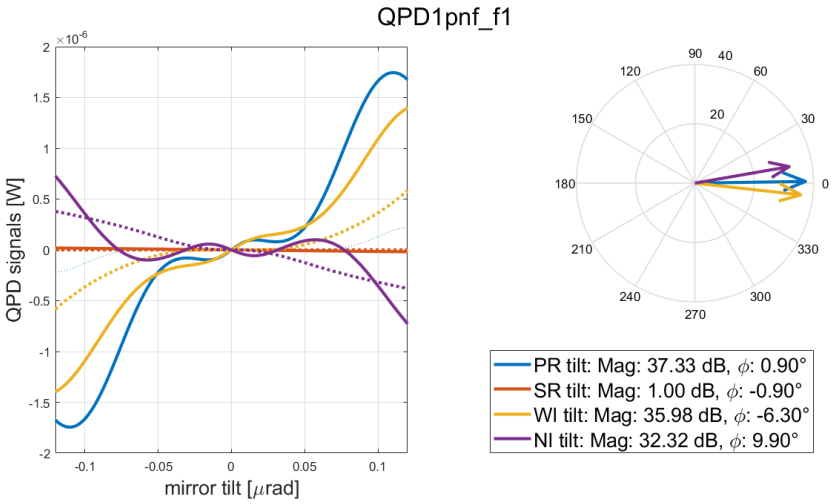

Figure 36: the simulated signals for QPD1nf_f1 with corresponding compass plot. Both components of the error signals are show (the quadrature components are dotted).

This is a bad error signal, since all the mirror tilts produce signals with very small linear regions. The signal for NI shows also five zero crossings in the swept region.

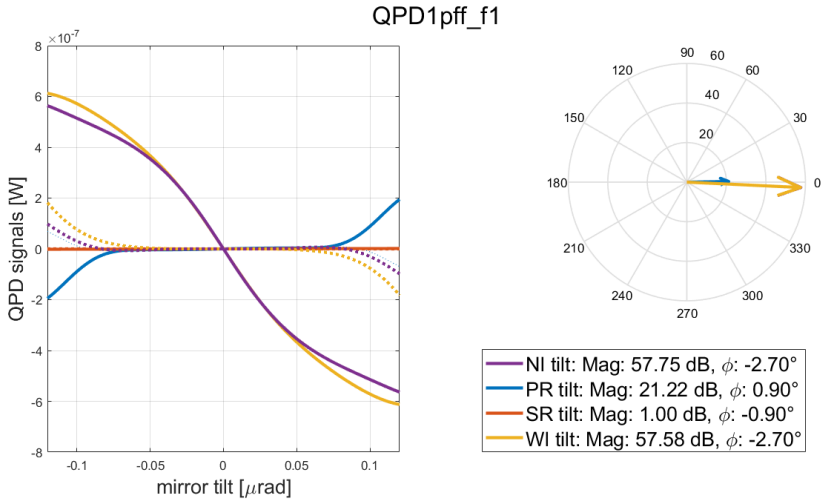

Figure 37: the simulated signals for QPD1ff_f1 with corresponding compass plot. Both components of the error signals are show (the quadrature components are dotted).

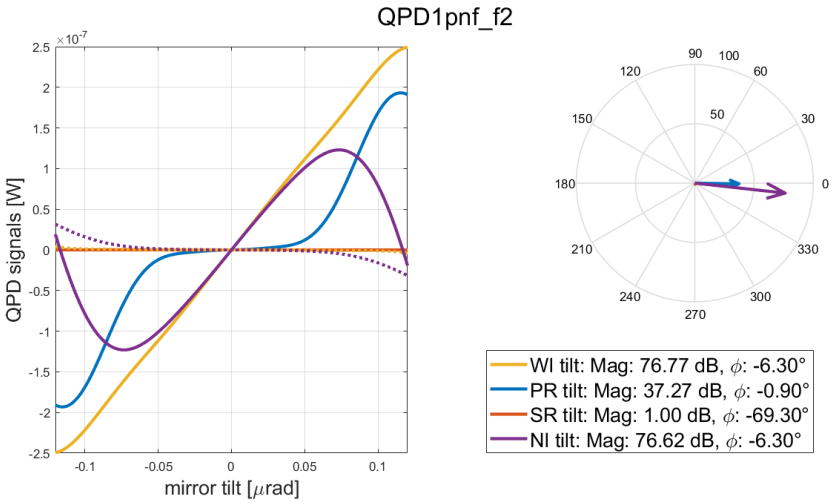

Figure 38: the simulated signals for QPD1nf_f2 with corresponding compass plot. Both components of the error signals are show (the quadrature components are dotted).

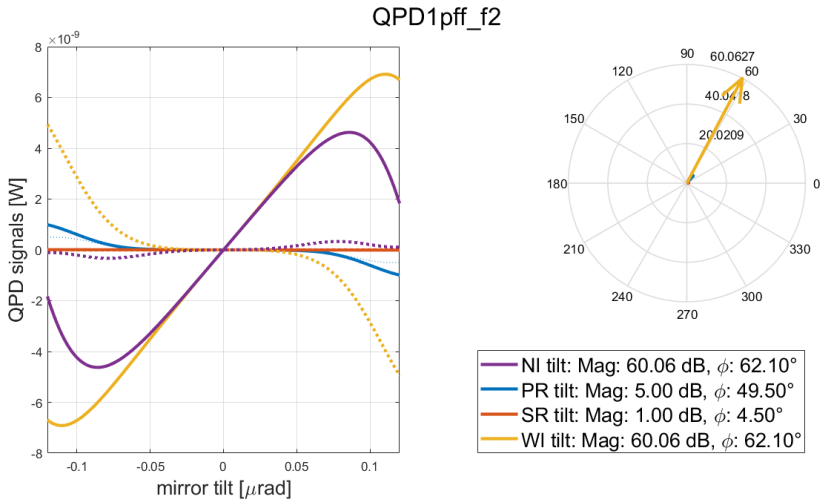

Figure 39: the simulated signals for QPD1ff_f2 with corresponding compass plot. Both components of the error signals are show (the quadrature components are dotted).

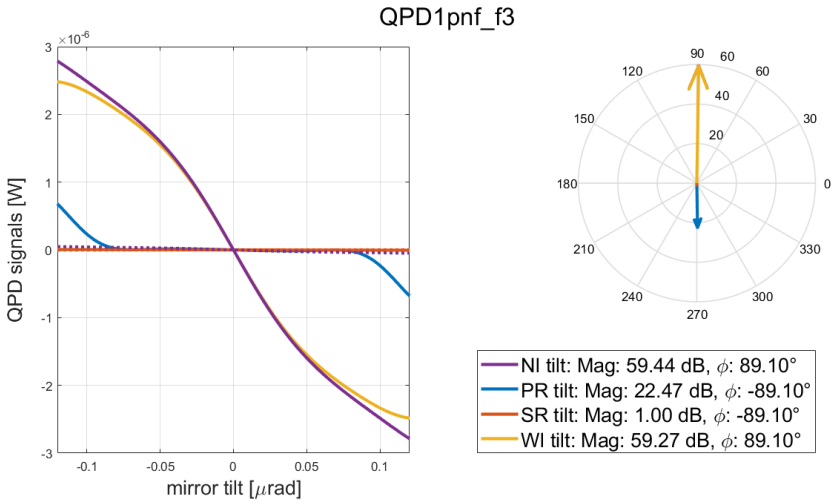

Figure 40: the simulated signals for QPD1nf_f3 with corresponding compass plot. Both components of the error signals are show (the quadrature components are dotted).

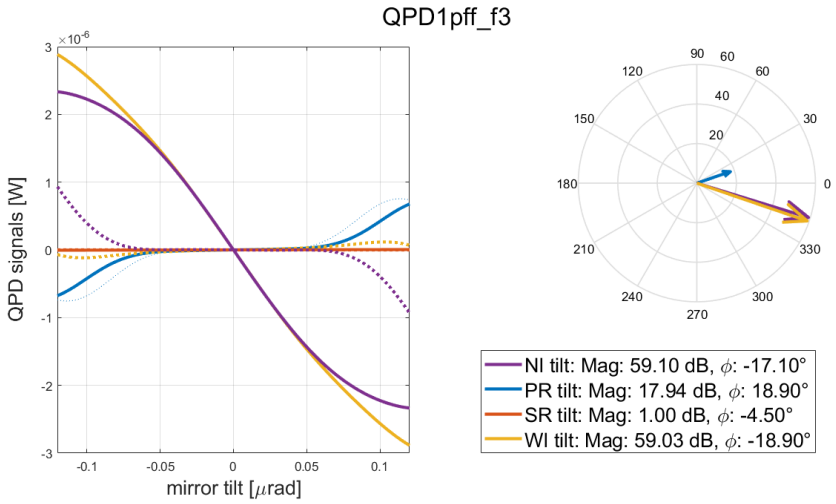

Figure 41: the simulated signals for QPD1ff_f3 with corresponding compass plot. Both components of the error signals are show (the quadrature components are dotted).

At a first glance, we can notice a common trend among the signals: all of the DoFs show a strong coupling on each of them, especially the PR with the ITMs. On some of them, like Figures 24 or 32, the optimal demodulation phase for the SR tilt is different from the others, which suggest at least a weaker coupling of the SR tilt with the other DoFs, but the SR tilt produces an error signal with a very small optical gain on every photodiode, and it basically disappears every time when confronted with the others.
This situation is not ideal: the strong coupling between the PR and the ITMs tilt on all the QPDs means that it will not be possible to build a diagonal sensing matrix using the signals as they are generated by the quadrants. We will have to construct a complex sensing that involves combination of the quadrant signals to isolate a specific DoF.

4.4 SR alignment: DC signals

To control the SR tilt, we could try and use the DC components of the photodiodes, shown in the following figures:

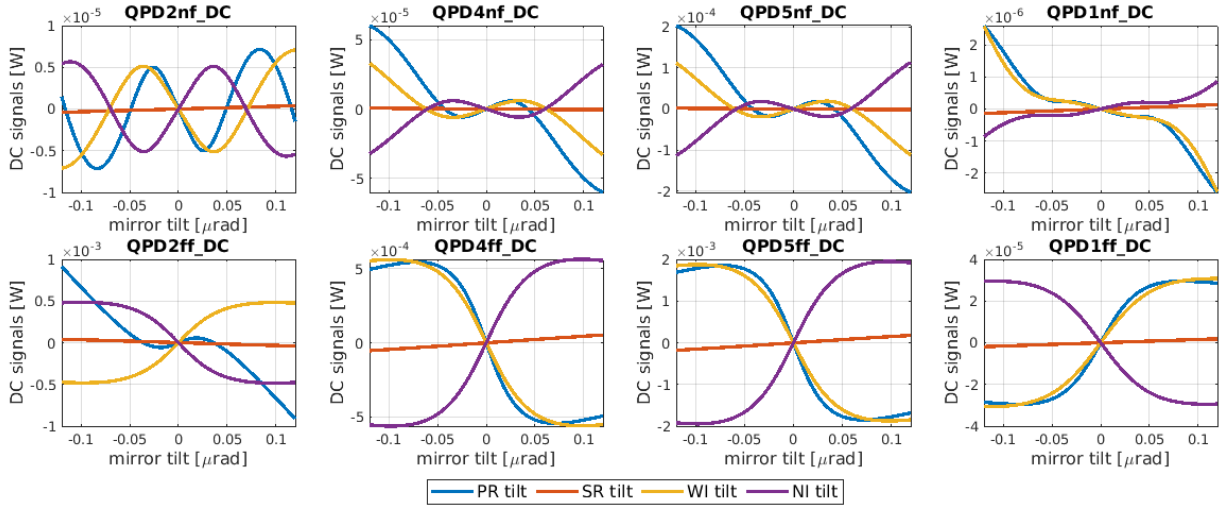

Figure 42: Simulated DC signals for each alignment DoF, on all of the implemented QPDs. Notice how the SR tilt always produce an error signal of negligible optical gain, when confronted with the ones produced by the other DoFs.

The SR mirror does not exhibit a good optical gain on any DC channels. While its slope around the origin is visible, for example on QPD4 and QPD5 far-field, the tilt of the all the other mirrors dominate these signals as well. It could be interesting to extend the tilt range of the SR to search for the limits of the linear region of its error signals, since, as we have seen so far, while the gain is low the signals always seems to be in their linear region

In the following plot we extend the tilt range of the SR to ± 2 μrad to search for the limits of the linear region of the error signals produced on the DC channels. The tilt of the SR causes a smaller fraction of the beam power to be scattered on the HOMs than it does for the other mirrors, and consequently the signals converge to their definitive shape after taking into account less modes in the simulation. Therefore it was possible to push the limit of the tilt range quite a lot without a severe increase in computational time.

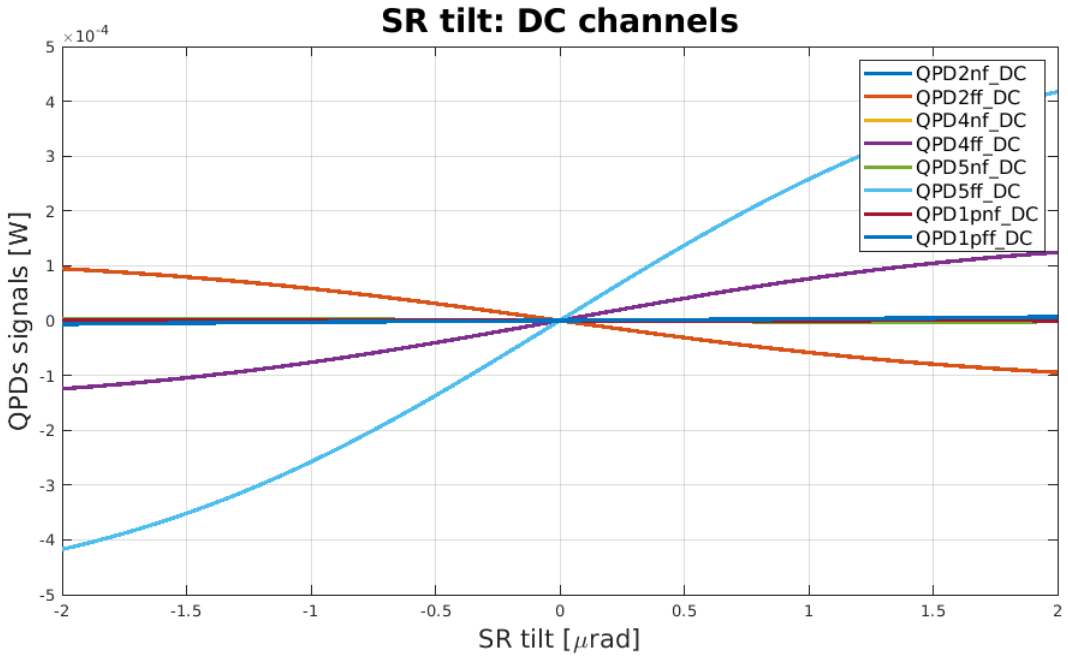

Figure 43: Simulated DC signals for QPD for a tilt of the SR mirror. Since this DoF generates less HOMs during its sweep, we were able to extend the tilt range to ± 2 μrad. Compared to the tilt of the other mirrors, which was confined in the ± 0.12 μrad range, the SR tilt has a much larger linear region on these signals, but the optical gain remains small, compared to the other mirrors on each quadrant.

5 Control scheme

As emerges from the simulation of the alignment error signals, it is impossible to build a diagonal sensing matrix for alignment of the CITF, due to the strong coupling among the DoFs on almost all the sensors, and also because the SR tilt produces error signals of very small optical gain.
This might not necessarily be a problem, since the current strategy for the lock acquisition is to align the cavity TMs with the IR and lock the arms with the green laser, and then lock the CITF. This means that the ITMs have already been aligned by the time one starts working on the CITF, and therefore the contribution of their tilt on each error signal we have shown so far can be ignored. If the need to align the ITMs persists at this stage, then the correction will be applied on BS tilt and PR transversal displacement to recover the correct orientation of the beam on the input mirrors, without touching them after locking the arms.
This is the current strategy for which, considering how small the SR signals are, we only have to align the PR mirror. We will also consider the case of the CITF aligned without the arms.

5.1 Current strategy: alignment of the PR

For this case all we have to do is gather the PR signals on Figs.18:41 and choose the one with the best optical gain and linear region. Since we have signals from a lot of quadrants to plot, to make a clearer plot we are going to initially show the root of their squared sum:

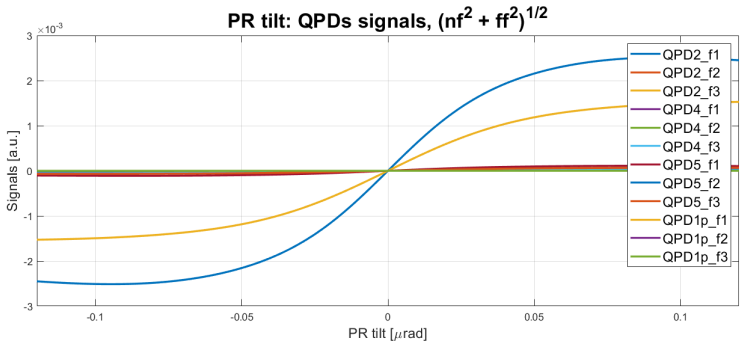

Figure 44: Root squared sum of the near-field and far-field quadrants' signals for a misalignment of the PR.

In this Figure one can see that QPD2_f1 is a clear winner, with double the optical gain than the second best. We can now show the near-field and far-field components of this square sum singularly:

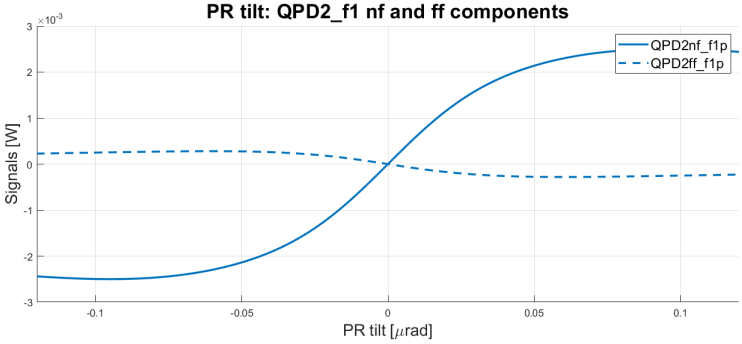

Figure 45: Root squared sum of the near-field and far-field quadrants' signals for a misalignment of the PR.

The QPD in near-field detects the greatest signal. `QPD2_f1_nf` is the best error signal for the PR alignment.

5.2 CITF stand alone case: alignment of PR and ITMs

If the solution to align the CITF were to align the PR and the ITMs without the support of the auxiliary laser, then one must deal with the strong coupling among them, omnipresent on the QPD signals. Thus, we are forced to take combination of these signals in the attempt to find some way to decouple the misalignment of on mirror at a time.

5.2.1 Error signal for PR misalignment

For the PR mirror there is a good combination given by `QPD4ff_f3`+10^3·`QPD4ff_f2`:

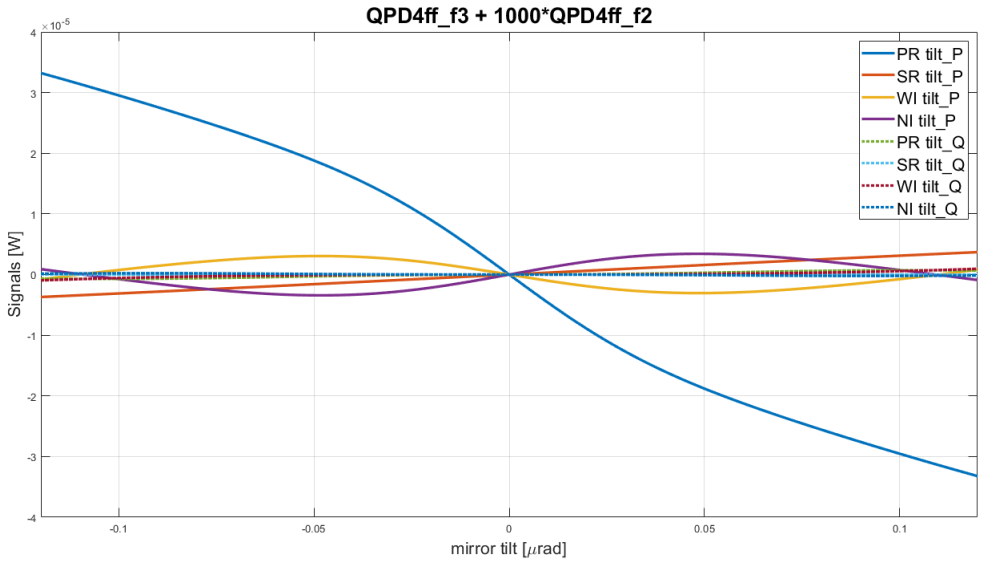

Figure 46: Complex error signal for the PR tilt given by `QPD4ff_f3`+10^3·`QPD4ff_f2`. Both in-phase (full lines) and quadrature (dotted lines) of the Ward signals are shown.

This composed signal shows a good optical gain, and the tilt of every other mirror produces a fairly flat signal in the linear region of the PR tilt. Overall, this seems to be a good choice.

5.3 Error signal for WI misalignment

For the WI mirror there is a good combination given by `QPD4ff_f3−24·QPD1pff_f1`:

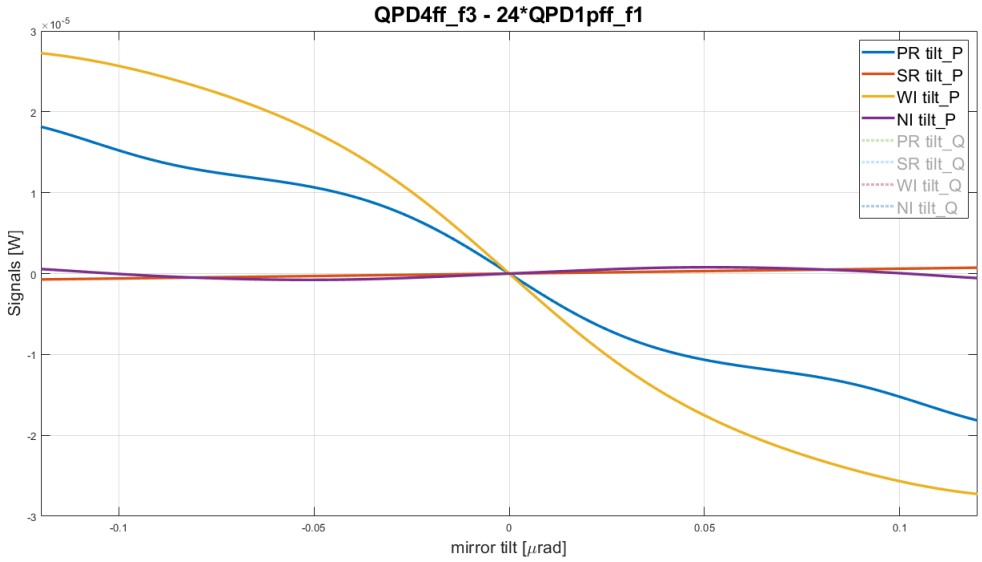

Figure 47: Complex error signal for the WI tilt given by `QPD4ff_f3−24·QPD1pff_f1`. Both in-phase (full lines) and quadrature (dotted lines) of the Ward signals are shown.

Notice that the error signal for WI is very well decoupled from the signal for NI, but strongly coupled with the signal for the PR. There is no escaping this: as we have seen in Figs.18:41, the PR is prominent on many QPDs. In any case, one can align the PR before the ITMs in order to decouple their error signals.

5.4 Error signal for NI misalignment

For the NI mirror there is a good combination given by `QPD4ff_f3`+24·`QPD1pff_f1`:

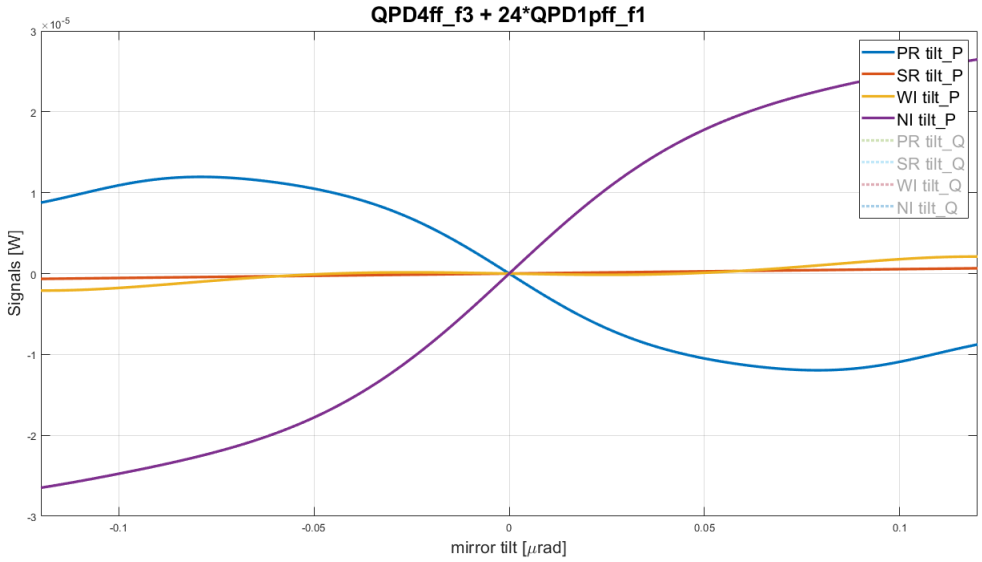

Figure 48: Complex error signal for the NI tilt given by `QPD4ff_f3`+24·`QPD1pff_f1`. Both in-phase (full lines) and quadrature (dotted lines) of the Ward signals are shown.

Notice that the error signal for NI is very well decoupled from the signal for WI, but strongly coupled with the signal for the PR. The same considerations done for WI are valid.

5.5 Sensing Matrix

We can now build the sensing matrix for these three combined error signals:

	PR	WI	NI	SR
QPD4ff_f3 + 1000 · QPD4ff_f2	**-0.4719e-3**	-0.1051e-3	0.1174e-3	0.0057e-3
QPD4ff_f3 - 24 · QPD1pff_f1	-0.3108e-3	**-0.4283e-3**	0.0210e-3	0.0061e-3
QPD4ff_f3 + 24 · QPD1pff_f1	-0.3044e-3	-0.0089e-3	**0.4489e-3**	0.0054e-3

Since we have concluded that there is no good error signal for the alignment of the SR, we are left with sensing matrix fairly diagonal for the other three mirrors. The coupling that we can notice on the second and third row between PR and WI/NI respectively can be dealt with by ??

6 Conclusions

We have built the simulation of the sensing for the angular control of the CITF. Our conclusions are:

- The misalignment of the SR produces an almost invisible error signal on every quadrant. We are forced to abandon the effort of aligning it and be satisfied with a pre-alignment using its local control, with the idea of completing the process in a later step of the lock acquisition.
- If the strategy of aligning the ITMs with the green laser is maintained, then only the PR is left to align. In this condition the signal given by QPD2nf_f1 has the highest optical gain.
- If the CITF has to be locked for a prolonged period of time without the arms, one has to rely on alignment error signals generated inside the CITF itself. In this case, PR, WI and NI have to be aligned with the quadrants. Given the strong coupling between them on all of the sensors, we had to build composed error signals for them. We have found a sensing matrix for this complex control scheme.

References

[1] Pykat website:
http://www.gwoptics.org/pykat/ 4

[2] GitHub repository for the lock routine:
https://git.ligo.org/IFOsim/Finesse_playground/-/tree/master/andreas_freise/2020/AdV 4

[3] D.Z.Anderson *Alignment of resonant optical cavities*, Applied Optics Vol.23 No.17, 1984 5

[4] E.Morrison, B.J.Meers, D.I.Roberston, H.Ward *Automatic alignment of optical interferometers*, Applied Optics Vol.33 No.22, 1994 14

[5] J.Casanueva *Control of the gravitational wave interferometric detector Advanced Virgo*, PhD thesis, Université Paris-Saclay, 2017 16